Lab on a Chip

Accepted Manuscript

This article can be cited before page numbers have been issued, to do this please use: A. Sonato, M. Agostini, G. Ruffato, E. Gazzola, D. Liuni, G. Greco, M. Travagliati, M. Cecchini and F. Romanato, *Lab Chip*, 2016, DOI: 10.1039/C6LC00057F.

ROYAL SOCIETY OF CHEMISTRY

www.rsc.org/loc

View Article Online
DOI: 10.1039/C6LC00057F

Surface acoustic wave (SAW)-enhanced grating-coupling phase-interrogation surface plasmon resonance (SPR) microfluidic biosensor

Sonato, A.[a, †]; Agostini, M. [b, c, †]; Ruffato, G. [d]; Gazzola, E. [d]; Liuni, D. [d]; Greco, G. [b]; Travagliati, M. [b, c] and Cecchini, M.* [b]; Romanato, F. [a, d]

[a] CNR-IOM, Area Science Park, S.S. 14, km 163.5, 34149, Basovizza (TS), Italy

[b] NEST, Istituto Nanoscienze-CNR and Scuola Normale Superiore, Piazza San Silvestro 12, 56127 Pisa, Italy

[c] Center for Nanotechnology Innovation@NEST, Istituto Italiano di Tecnologia, Piazza San Silvestro 12, 56127 Pisa, Italy

[d] University of Padova, Department of Physics and Astronomy, Via Marzolo 8, 35131 Padova, Italy

[†] these authors contributed equally

*marco.cecchini@nano.cnr.it

Abstract

A surface acoustic wave (SAW)-enhanced, surface plasmon resonance (SPR) microfluidic biosensor in which SAW-induced mixing and phase-interrogation grating-coupling SPR are combined in a single lithium niobate lab-on-a-chip is demonstrated. Thiol-polyethylene glycol adsorption and avidin/biotin binding kinetics were monitored by exploiting the high sensitivity of grating coupling SPR under azimuthal control. A time-saturation binding kinetics reduction of 82% and 24% for polyethylene and avidin adsorption was obtained, respectively, owing to the fluid mixing enhancement by means of the SAW-generated chaotic advection. These results represent the first implementation of a nanostructured SAW-SPR microfluidic biochip capable of significantly improving the molecule binding kinetics on a single, portable device. In addition, the biochip here proposed is suitable for a great variety of biosensing applications.

1. Introduction

Since their first demonstration in the early 1980s, surface plasmon resonance (SPR) sensors have been widely recognized as useful tools for detecting chemical and biological species, and attracted a rapidly growing interest in the past two decades owing to their high sensitivity, label-free operation and possibility of real-time detection[1,2]. The most common strategies adopted for SPR sensing include prism-coupling (PC-SPR Kretschmann geometry), optical waveguide, optical fiber and grating-coupling (GC-SPR)[2]. Recent works have suggested that a turning point in SPR sensor research would be the combination of SPR strategies with other technologies in order to improve integration and plasmonic sensitivity[3]. Ouellet *et al*. realized an SPR device consisting in 264 element-addressable chambers for volumes of 700 pL[4] and Chen *et al.* demonstrated the capability of a nanoplasmonic biosensor microarray in detecting concentrations down to 5-20 pg/mL in a 1 µL serum sample within 40 minutes[5]. Although these techniques show many advantages and have led to the commercialization of portable and efficient SPR instruments, SPR systems often suffer from low throughput and bulky detection equipments[6], limiting SPR-sensor applications[3]. In this light, microfluidics is the ideal solution to these limitations. By properly designing microfluidic biochips it is

View Article Online
DOI: 10.1039/C6LC00057F

possible to miniaturize the analyte-sensitive areas with an overall reduction of the chip dimension, downscale the liquid reagents and sample volume, improve automation, and increase the number of experiments in a single biochip by multiplexing approaches [7–10]. However, as the fluidic channel dimensions approach the micron scale, laminar flows become dominant owing to the low Reynolds number that typically characterizes microfluidics. In these environments mixing times are usually determined by diffusion alone, which can be prohibitively long and leads to long-lasting biochemistry experiments [11]. An elegant method that has been introduced to overcome these issues is to actively perturb the liquid laminar flux by exploiting surface acoustic waves (SAWs). SAWs are a powerful technology that in the past two decades was introduced either for microfluidics [12] and sensing purposes[13–17]. By exploiting their ability to transfer a large amount of momentum into fluids –which generates acoustic streaming[18]– one can perform several tasks, such as moving droplets [19,20], heating fluids [21,22], pumping liquids in microchannels [23,24], and, importantly, generating efficient mixing [25,26]. All of these tasks can be performed in low power consumption, portable, battery-operated systems.

The potential of SAW-SPR coupling has been previously explored only by Renaudin *et al.*[27] with biochips not based on microfluidics. This interesting paper reported enhanced biotin-streptavidin binding kinetics in the presence of SAWs, but the authors did not decouple the actual effect of SAW streaming from the contribution of the heating originating from radiofrequency (RF) dissipation and SAW damping on the chip [22,28].

Here, we demonstrate a new approach for SPR biosensing based on the combination of microfluidics, SAW-mixing and the innovative real-time phase-interrogation grating-coupling SPR technology, that has been previously demonstrated as a promising technology in term of detection sensitivity, setup scalability and throughput [29–33]. This configuration comprises a negative-control area for the evaluation of the heating effect on the biosensing process. On a single lithium niobate (LN) substrate the nanostructured SPR sensing areas, the interdigital transducer (IDT) for SAW generation and the polydimethylsiloxane (PDMS) microfluidic chambers were fabricated using standard, reproducible and high throughput micro- and nano-fabrication techniques. SAWs are exploited for inducing chaotic advection inside the chamber and enhancing fluid mixing. The SPR detection is based on surface plasmon polariton (SPP) excitation via gold metallic grating upon azimuthal orientation and phase interrogation here applied to real-time SPR sensing for the very first time in combination with SAW microfluidics. In addition, a portable bench detection setup was realized and a dedicated software was developed for data acquisition and data processing. All grating geometrical parameters and SPP excitation conditions were opportunely chosen based on theoretical calculations. We benchmarked the biochip against the avidin/biotin assay, exploiting a thiol-polyethylene glycol (biotin-PEG_{2kDa}-SH) layer as non-fouling coating[34,35], and we showed accelerated reaction kinetics.

View Article Online
DOI: 10.1039/C6LC00057F

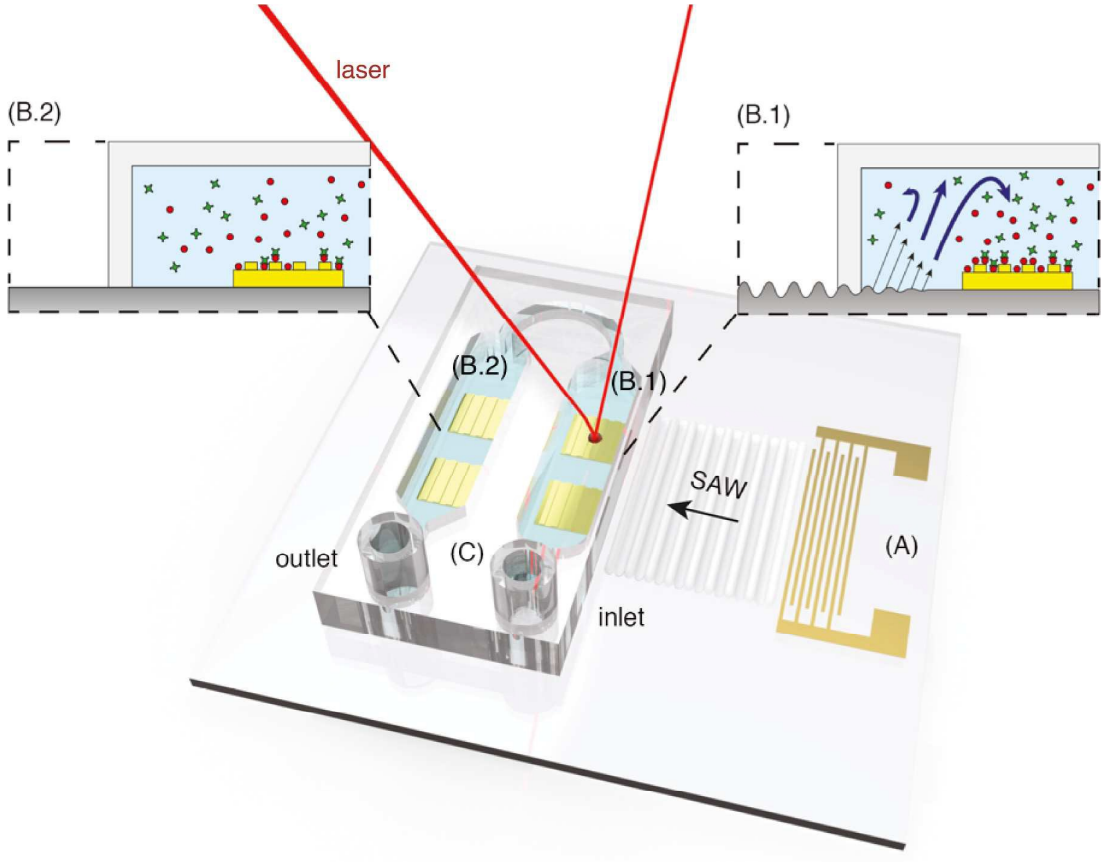

Fig. 1 Schematic overview of the acousto-plasmonic device on the LN substrate, characterized by three main parts: an IDT for Rayleigh SAW generation (A), 4 nanostructured SPR sensing areas (B) and a PDMS microchannel with two microchambers (C). The two microchambers are designed such that the SAWs affect only B.1, while they are fully damped before reaching B.2. In the inset, the binding kinetics mechanisms in the SAW-driven (B.1) condition and in the control chamber (B.2) are depicted.

2. Experimental

Biochip fabrication

The biochip was designed in order to obtain four SPR nanostructured areas of which only two were affected by SAW mixing (**Fig. 1**). The fabrication procedure consisted in LN patterning and sensor chip assembling. LN patterning (**Fig. 2**) was performed in two steps: pads and IDT fabrication (A), and SPR area patterning (B).

Pads and IDT fabrication (**Fig. 2(A)**). LN substrates were cleaned in a milliQ water-soap solution, rinsed in acetone and isopropanol (IPA), immersed in a H_2SO_4:H_2O_2 (3:1) solution for 10 minutes, rinsed thoroughly with milliQ water and IPA, dried under nitrogen flux and then exposed to plasma oxygen cleaning (90 W for 20 s). The cleaned substrates were coated with an adhesion promoter (HMDS - Microchem) upon spin coating at 2000 rpm for 30 s and then a positive photoresist (MICROPOSIT^{TM} S1813^{TM} – Microchem) was spun onto the substrate (4000 rpm, 30 s). After soft baking (80°C, 1h) the substrates were then exposed to UV light for 10 s (Karl Suss MJB3 Mask Aligner) and developed in MF-319 (MICROPOSIT^{TM}) for 2 min, using an optical mask with the sensor chip design (**Fig. 2(A.1)**). A 100 nm-gold layer was deposited (RIAL EGE 450 electron beam evaporator) and a 10 nm-chromium layer was deposited between LN and gold in order to

View Article Online
DOI: 10.1039/C6LC00057F

improve the metal stability. The final structures were obtained after a final lift off process in acetone (**Fig. 2(A.2)**).

SPR sensing area fabrication (**Fig. 2(B)**). S1805 (MICROPOSIT™) diluted into propylene glycol monomethyl ether acetate (PGMEA) (Microresist Technology) (2:3) was spun onto the patterned substrates (4000 rpm, 30 s). After soft baking (80°C, 1h) the samples were exposed to Laser Interference Lithography (LIL) (lab-made Lloyd configuration LIL setup; He-Cd laser 325 nm) with an exposure dose of 77mJ/cm^2 and an incidence angle of 24°. Development was performed in MF-321 (MICROPOSIT™) for 20 s (**Fig. 2(B.1)**). A silicon stencil was fabricated starting from the available optical mask in order to obtain the desired plasmonic nanostructure only in the dedicated square gold patches. A silicon nitride membrane was fabricated using UV photolithography and KOH-etching and the membrane was etched via reactive ion etching. This stencil was put in contact with the sample and then aligned with the four gold patches previously fabricated. This assembly was then exposed to a 35 nm-gold evaporation source (**Fig. 2(B.2)**) and the desired layer of gold was thus deposited only in the area exposed by the stencil. Finally, a lift-off process in acetone was performed obtaining the final desired metal nanostructures.

Sensor chip assembling. Microchannels, fabricated in PDMS (SYLGARD® 184) by replica molding, were covalently bonded onto the chip. We used PDMS owing to its transparency, which is needed for performing particle velocimetry analysis, easy and low-cost manufacturing by soft-lithography techniques, straightforward possibility of tuning its acoustic properties by changing the elastomer-curing agent volume ratio, and its biocompatibility. The LN substrate and the PDMS surface were activated with oxygen plasma (FEMTO, Diener, Germany) @40 W for 1 minute, aligned using an optical microscope, and finally baked for at least 1.5 hours at 80 °C in an oven for a complete bonding.

View Article Online
DOI: 10.1039/C6LC00057F

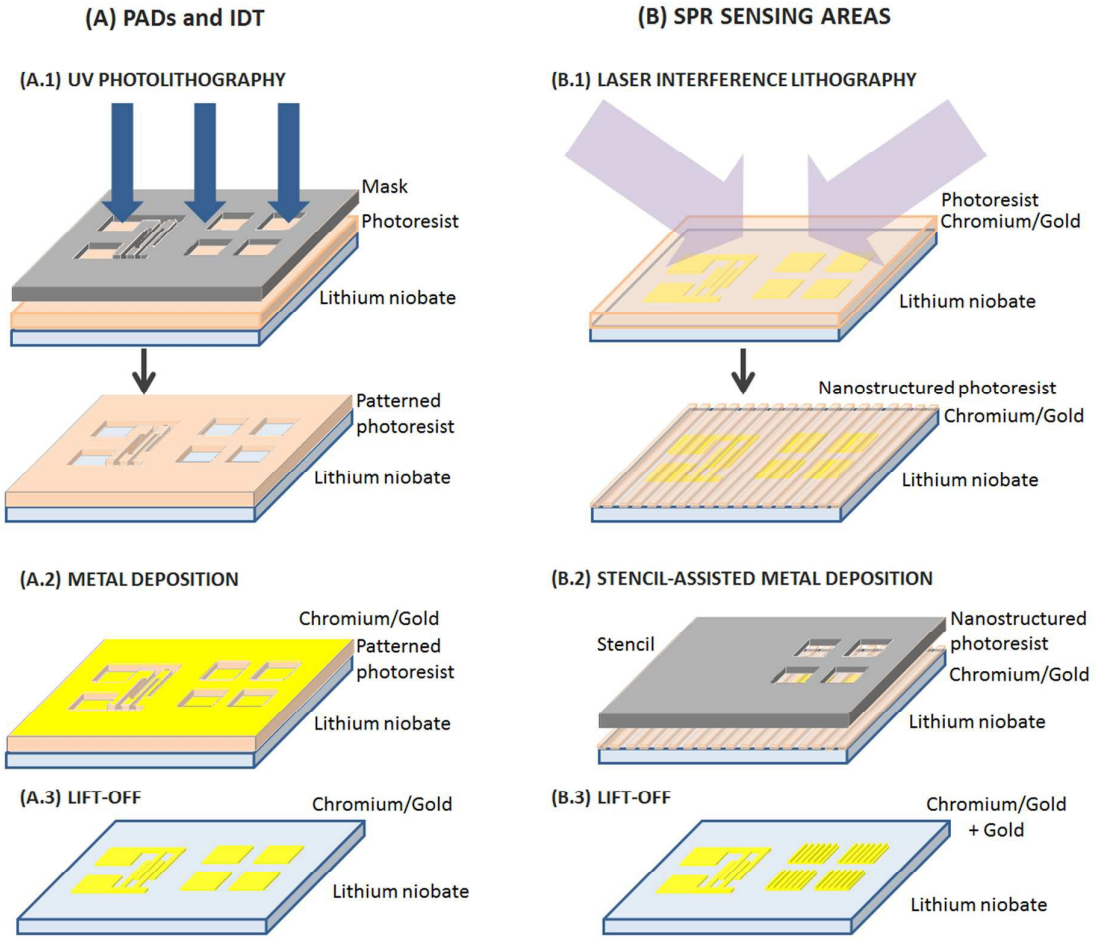

Fig. 2 Acousto-plasmonic device fabrication procedure. The first step was the fabrication of the gold pads and IDT (A) by combining UV photolithography (A.1), metal evaporation (A.2) and lift-off (A.3) processes. For SPR sensing area fabrication (B) nanopatterning by LIL was performed on the whole device surface (B.1). Using a silicon stencil, gold was deposited only onto the four areas dedicated to SPR (B.2) so that lift-off allowed us to obtain the final plasmonic nanostructures in the areas of interest (B.3). Optical microscope and scanning electron microscopy (SEM, ZEISS SUPRA 40, 2kV-EHT) were used for IDT, pads and nanostructures morphology characterization.

SAW excitation and detection

In our device, the generated SAWs are Rayleigh waves, that are elastic waves which propagate along the surface of a crystal with a polarization in the sagittal plane [36,37]. In our experiments they are excited by applying an RF signal to an IDT patterned on a 128° Y-cut, X-propagating LN substrate, **Fig. 1(A)**. The IDT comprises 19 pairs of fingers of 40 µm periodicity (p), 50% metallization ratio and 5 mm acoustic aperture. SAW excitation frequency f_{SAW} is given by the ratio $\frac{v_s}{2p}$, where v_s is the SAW velocity along the substrate surface and $2p$ is the same as the SAW wavelength λ_{SAW}. Our device was designed to excite a nominal 50 MHz wave and was tested by measuring the power reflection coefficient as a function of the frequency

View Article Online
DOI: 10.1039/C6LC00057F

with a vector network analyzer (ENA Series Network Analyzer, E5071C, Agilent Technologies). The actual SAW resonance frequency was 47.8 MHz. SAW amplitudes were measured against SAW power using a laser Doppler vibrometer (UHF-120 Ultra High Frequency Vibrometer, Polytec, Germany); a 100-point line average was used to account for any lateral variation of the SAW amplitude. After characterization, SAWs were excited by applying a voltage sine wave at 47.8 MHz to the IDT at different power levels using an RF generator (MXG Analog Signal Generator N5181A, Agilent Technologies) connected to an amplifier (ZHL-5W-1, MiniCircuits).

Fluid dynamics study

For fluid flow visualization, we loaded the chip with milliQ water containing 500 nm latex beads (L3280, Sigma-Aldrich) at the concentration of 7.6×10^8 particles/ml and acquired 30 fps videos by using a brightfield inverted microscope (Eclipse TI, Nikon, Japan) equipped with a 4x objective and CMOS camera (A602-f, Basler, Germany). For visualization of the streamlines, we normalized the contrast of each frame, subtracted the time-averaged image in order to remove static objects, and finally superimposed all the collected frames using Fiji. To quantify the fluid velocity field, we analyzed the data with an ensemble-correlation micro particle image velocimetry (μPIV) code (Prana PIV, Virginia Polytechnic Institute and State University, 2012) on the gold SPR areas. The data images were then stitched by aligning the resist markers that were patterned during chip fabrication.

SPR detection setup

For the SPR generation, a numerical code base on Rigorous coupled-wave analysis (RCWA)[38] was implemented in order to compute the theoretical reflectivity as a function of the incidence polar angle θ and increasing values of the digital grating depth. Simulations were performed in water environment for incident wavelength λ = 635 nm at p-polarization (TM mode)[39]. For 400 nm-pitch and duty cycle 0.5, 35 nm-amplitude digital gold gratings were predicted as the optimal choice for maximizing plasmonic coupling and therefore minimizing reflectance value at resonance (for details see Supporting Information #S.I.2). A bench custom phase-interrogation SPR setup composed by a SPPs excitation and detection part, a heating sample holder connected to a temperature controller and a dedicated software, were used. The phase-SPR working principle and the setup are shown in **Fig. 3**. An incident light beam (635 nm-wavelength; Thorlabs, Inc.; < 5.0 mW of output power; class 3R), after passing through a polarizer (Thorlabs, Inc: LPVISE100-A) and through a rotating half-wave plate (Thorlabs, Inc: LPVISB100-MP) mounted on a motorized rotation stage (Thorlabs, Inc: PRM1/MZ8E), reached a translating sample holder (Edmund: 56-794, Thorlabs, Inc: DT25/M) mounted onto a goniometer (Thorlabs, Inc: GN18/M) and a metric rotation stage (Edmund: NT55-028). The light reflected by the SPR sensing platform positioned onto the sample holder was collected by a CMOS camera (Thorlabs, Inc: DCC1545M). The polarizer and the half wave plate were mounted on a vertical rotation stage (Thorlabs, Inc: SL20/M, C1525/M, P14). For temperature controlled experiments a custom setup was realized. The system was composed of a thick aluminum plate heated by a pair of aluminum encased 50W power resistors. A Ø1.5mm type K thermocouple has been fitted within the aluminum plate at 2 mm below the surface on which the sample is placed (see Fig. 3(a), element C). A digital controller set the low voltage DC power supply to the resistors upon a feedback loop based on said thermocouple. The temperature could be set between 25 to 100°C with a ±1°C stability. A custom software was realized using Microsoft Visual Studio C++ 2012, National Instruments Measurement Studio Visual C++ MFC and the ActiveX provided by Thorlabs, Inc for the management of the motor, the polarizer and the CMOS digital camera. The software allowed experimental parameter setting, real-time measurements and data

View Article Online
DOI: 10.1039/C6LC00057F

processing. For data processing, raw data were processed in order to obtain a sensor response in arbitrary units, from 0 to 1.

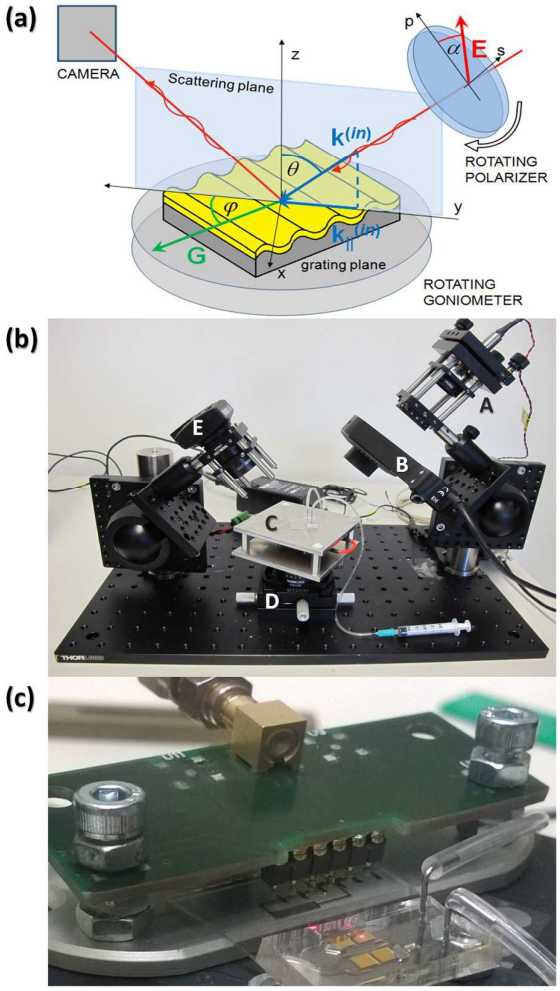

Fig. 3 SPR working principle and detection setup. **(a)** Phase-interrogation SPR (adapted from Romanato, F.[33]). The plasmonic substrate is mounted onto a rotating goniometer allowing the azimuthal control of the grating plane. A fixed-wavelength laser beam, after passing through a polarizer, is reflected by the nanostructured surface and reaches a CCD camera. During the polarization-modulation analysis, polar and azimuthal angles (ϑ , φ) are kept fixed in correspondence of the plasmonic resonance and a polarization scan of the angle α is performed (see Supporting Information #S.I.1 for details). **(b)** The bench detection setup (H= 35 cm; L= 45 cm; W= 40 cm) was composed by a laser (A), a polarizer (B), a heating sample holder (C) that could be translated and azimuthally rotated (D) and a CMOS camera (E). **(c)** Configuration for the SAW-driven experiments.

View Article Online
DOI: 10.1039/C6LC00057F

Sensing experiments

A 2 mM aqueous solution of biotin-PEG_{2k}-SH ($bPEG_{2kDa}$ –SH; NANOCS) in milliQ water was loaded in the microfluidic chamber for 5, 15 and 24h in the experiments with SAWs, without SAWs at 32°C and without SAWs at 20.4°C respectively. After bPEG-SH deposition, the surface was rinsed thoroughly in milliQ water and in 10 mM phosphate-buffered saline (PBS). A 500 nM avidin (Sigma Aldrich) solution in PBS 10 mM was then left in the incubation chamber for 3h. Finally, the sample was rinsed in 10mM PBS. PTFE tubes (Masterflex Tygon E-3603, Cole Parmer, Italy) and 1 ml syringes (Benefis srl, Italy) were used to inject liquid into the microchannels. Our device worked in stop-flow, meaning that there wasn't any net fluid motion inside the chamber during the SPR measurements. After the first experiment the sensor chip was re-generated: the microfluidic chamber was carefully removed by using a cutter, and then the surface was cleaned with piranha solution for at least 1h for an accurate removal of residuals. A further plasma oxygen step ensured thorough cleaning of the surface from previous functionalizations [13]. After the cleaning process new microfluidic channels were assembled onto the sensor surface, as previously described. For SAWs-driven experiments the PEG solution was inserted after 10 min from SAW generation in order to get a stable temperature inside the chamber. SAWs were kept on for the whole experiment duration. Real-time measurements were performed in the polarization range 0-180° with 1° and 2° step for the biotin-PEG-SH and avidin binding respectively; the time between each step and between each scan was set as 0.5 and 1 s respectively.

3. Results and discussion

The sensor chip fabricated is shown in **Fig. 4**. The fluid dynamics and the biosensing kinetics were investigated in order to fully characterize our novel device. Before evaluating the sensing performance, we analyzed in details the fluid behavior inside the microchannel, in order to maximize acoustic streaming and minimize parasitic effects such as heating: at this aim, we studied for different SAW generation parameters the chip temperature, and used µPIV analysis to measure the velocity fields and streamlines.

After having identified the optimal configuration of the SPR-SAW biochip, we proceeded with the biotin-PEG_{2kDa}-SH and the avidin/biotin biosensing process. Several biochips were fabricated and studied, and all of them showed quantitatively similar characteristics. All data shown in the following refer to one representative device, for which the fluidic and sensing characteristics have been systematically analyzed. Each chip has been used twice upon a thoroughly cleaning procedure consisting in the combination of both wet (*i.e.,* piranha solution) and dry (*i.e.,* oxygen plasma) techniques.

View Article Online
DOI: 10.1039/C6LC00057F

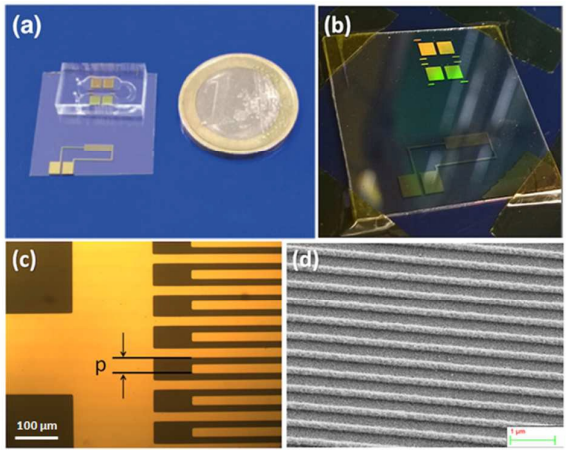

Fig. 4 Acousto-plasmonic sensor chip. The final biochip is shown in (a) whereas the four SPR sensing areas and SAW generating IDT just after their fabrication on the LN substrate are shown in (b). 40µm-periodicity *p* IDT and plasmonic grating (400nm-pitch and 35nm-amplitude) morphologies were characterized using optical microscopy (c) and SEM (d) respectively. The biochip was designed in order to get the SAW mixing effect only on the nanostructured areas positioned next to the IDT.

SAW fluidic and thermal characterization

Travelling SAWs are very sensitive to the presence of materials (fluids, plastics, metals, etc., hereafter called obstacles) on the surface along which they propagate. When an obstacle is placed on the SAW propagation path, the elastic wave scatters into it at the Rayleigh angle $\theta_R = \arcsin\left(\frac{v_s}{v_o}\right)$, where v_s is the SAW velocity and v_o is the speed of sound in the obstacle. In the case of a liquid obstacle, the radiated wave generates a pressure wave at the Rayleigh angle whose dissipation causes a strong chaotic advective phenomenon called acoustic streaming [18]. In our device this phenomenon is exploited to enhance the liquid mixing inside the detection microchamber, otherwise driven by diffusion alone and therefore slow. At the substrate-obstacle interface the SAW is exponentially attenuated owing to its power leakage into the material, becoming a Leaky SAW (LSAW). LSAWs are characterized by an attenuation length $x_{LSAW} = 0.45\frac{v_s\rho_s}{v_f\rho_f}\lambda_{SAW}$ [40], where ρ_s and ρ_f are the substrate and fluid density, respectively. Our device was designed such that the wave was acting only on the fluid in the first chamber (**Fig. 1-B1**), whilst, as the wave is exponentially attenuated, the second chamber remains unaffected (see ESI video) except for a parasitic heating effect due to the RF SAW generation and elastic wave viscous dissipation into both the PDMS and liquid[28]. Both the streaming and heating phenomena were fully characterized in order to discern their effects on the binding kinetics.

The fluid dynamics study results are shown in **Fig. 5** for 400 pm, 600 pm, 800 pm SAW amplitudes. The SAW-generated acoustic streaming creates a complex streamline pattern that allows the liquid inside the chamber to be mixed faster than by diffusion alone[41]. As expected, by increasing the SAW amplitude we measured a higher average and maximum particle velocity (**Tab. 1**), however we avoided higher power levels for preserving the chip integrity and limiting the heating effect. The chosen SAW amplitude for the

View Article Online
DOI: 10.1039/C6LC00057F

following experiments was 800 pm, at which the fluid reached a maximum velocity of 1530 ± 80 µm/s with an average value of 160 ± 40 µm/s in the gold SPR area regions. The streamlines structure does not qualitatively vary by changing the SAW amplitude. It is possible to identify two main lateral vortices and a central jetting zone, similarly to other fluid-dynamics reported for liquids interacting with SAWs (see, for example, [24]). A unique feature of this design with respect to the SAW-driven acoustic streaming pattern reported in literature is the presence of the two slower central back rolls.

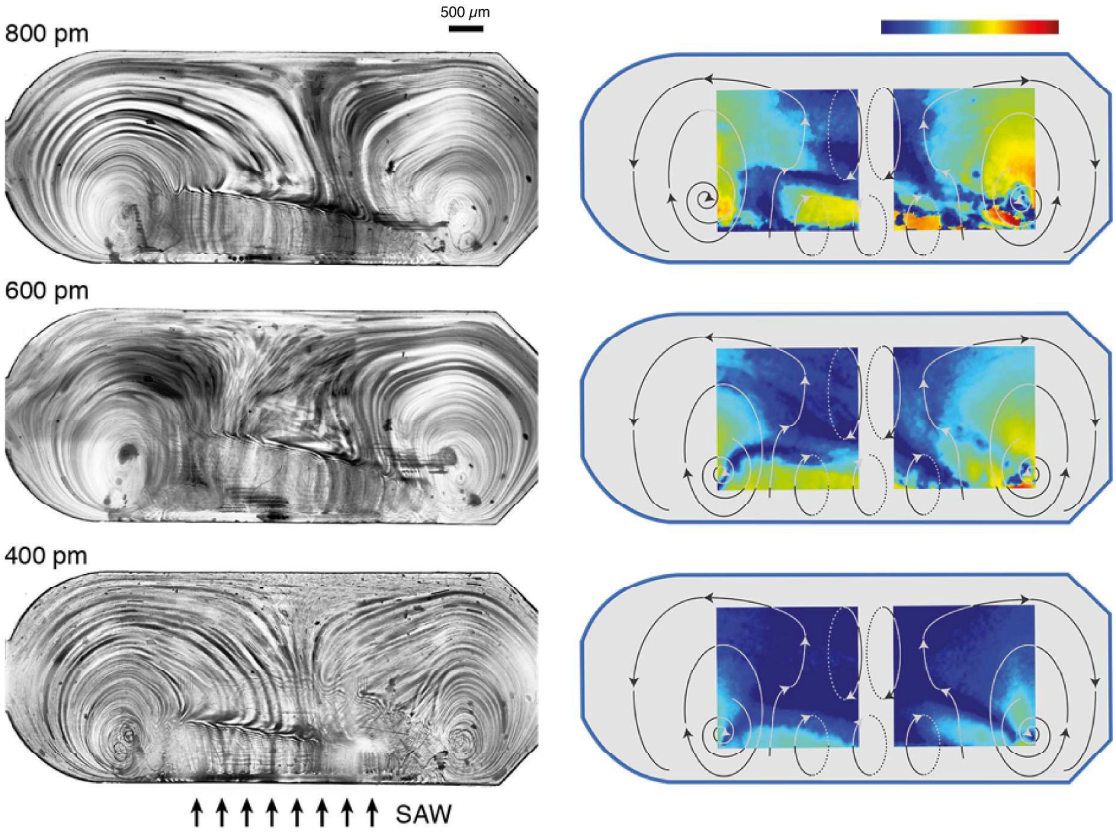

Fig. 5 SAW-induced streaming characterization for different wave amplitudes. Left side shows the streamlines of the flow caused by the SAW scattering inside the fluid and the subsequent acoustic streaming generation. Right side depicts the µPIV velocity fields for the corresponding wave amplitude on the two gold areas for SPR generation and analyte detection. Color bar represents logarithm of the velocity and ranges form 10 µm/s to 1800 µm/s.

	Average velocity (µm/s)		**Maximum velocity (µm/s)**	
SAW amplitude (pm)	**Left area**	**Right area**	**Left area**	**Right area**
400 pm	$(1.9 \pm 0.1) \times 10$	$(2.7 \pm 0.6) \times 10$	$(1.2 \pm 0.1) \times 10^2$	$(3.5 \pm 0.1) \times 10^2$
600 pm	$(5.9 \pm 0.2) \times 10$	$(8.6 \pm 0.1) \times 10$	$(2.6 \pm 0.3) \times 10^2$	$(5.7 \pm 0.3) \times 10^2$
800 pm	$(1.4 \pm 0.2) \times 10^2$	$(1.8 \pm 0.1) \times 10^2$	$(8.3 \pm 0.7) \times 10^2$	$(1.53 \pm 0.08) \times 10^3$

Tab. 1 Flow velocity measurements on the two SPR areas. Reported velocities are obtained by µPIV analysis, as shown in **Fig. 5**, collected on the gold areas. The wide range of velocities mirrors the chaotic behavior of the flow that causes mixing.

View Article Online
DOI: 10.1039/C6LC00057F

We also monitored the chip temperature by a thermal camera (FLIR A655sc with macroscopic lens) during each experiment. We selected the region-of-interest (ROI) of the recorded video on top of the PDMS microchannel, and registered the temperature variations from the chip basal temperature (20.4 °C). A temperature graph, representative of the experiments, is shown in **Fig. 6**. From the switching on of the signal generator (time = 0) the temperature rapidly increased (O(5 min)), reaching the steady-state value of ≈ 12 °C higher than the starting temperature. The isolated temperature drops stem from fresh liquid injection inside the microchamber. Owing to this temporal behavior of SAW-induced heating, every SAW-SPR measurements was performed after initially waiting for the chips to reach thermal equilibrium (≈ 10 minutes).

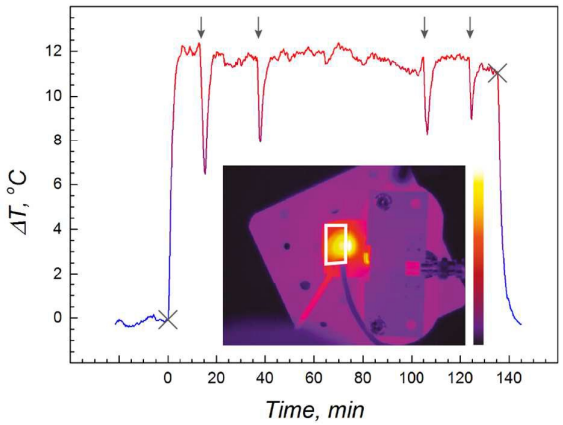

Fig. 6 Differential temperature $\Delta T = T - 20.4$ °C versus time during a representative experiment; SAW was turned on at time = 0 and switched off ≈ 135 minutes later (grey crosses); drops of temperature originate from liquid change inside the microchambers (grey arrows). Inset: Heating map at t ≈ 110 minutes. ROI was set on top of the PDMS microchannel as highlighted by the white rectangle. Color bar ranges from 18.8 °C to 34.1 °C.

A sensor calibration as a function of temperature and SAW generation was performed in the presence of the buffers adopted for sensing experiments to monitor SPR response variation due to dielectric temperature changes[42] (For details see Supporting Information #S.I.3).

Biosensing kinetics

We studied the binding kinetics of two different biosensing events: the adsorption of biotin-PEG_{2kDa}-SH onto the gold SPR gratings and the avidin/biotin binding. It is important to monitor both the avidin and the biotin-PEG binding as both of them must be considered parts of the whole sensing experiment. PEG is a polymer well-known for its non-fouling behavior and fundamental role in protecting the sensor surface from non-specific adsorptions due to the analyte itself or to contaminants of the analyte-containing solutions[34,35]. Among all PEG derivatives, thiol-PEG_{2kDa} was selected as its protection from non-specific adsorption onto our SPR sensors was previously demonstrated to be almost full in the presence of bovine

View Article Online
DOI: 10.1039/C6LC00057F

serum albumin and goat serum[34]. Although the advantages shown by PEG_{2kDa} are significant, the time required to obtain a PEG-fully covered corrugated sensor surface is relatively high as it ranges from 10 (*i.e.,* overnight deposition) to 24 hours[43–45]. On the contrary, avidin/binding kinetics is rapid owing to the protein high affinity and the binding event occurs in a range of about 30-60 minutes[34]. In this work we examined three binding kinetics configurations: (1) in the absence of SAWs at 20.4°C (*i.e.,* w/o SAWs@20.4°C); (2) in the absence of SAWs at 32±1°C (*i.e.,* w/o SAWs@32°C) and (3) in the presence of SAWs. The second condition was introduced as negative control since a temperature increase of 12°C occurred when the SAWs are switched on. A temperature of 32°C was chosen for all the temperature-driven experiments as it is the typical temperature reached by our sensor upon SAW generation, as shown in **Fig. 6**. SPR binding kinetics measurements were performed after thermal equilibrium was reached, 10 minutes after the SAWs were switched on. Continuous SAWs were excited for the whole experiment duration.

All the experiments started with the injection of milliQ water inside the microfluidic circuit. After $bPEG_{2kDa}$ -SH injection into the microfluidic chamber, SPR response rapidly increased until reaching the saturation when fully coverage of the nanostructures by $bPEG_{2kDa}$ -SH occurred. After having thoroughly rinsed the sensor surface with milliQ water, PBS and then avidin solution were injected. When the SPR response due to avidin binding had reached its saturation value, a sensor rinsing in PBS was performed. Raw phase shift data were processed in order to obtain a sensor response in the 0-1 range, where 0 represents the starting point (*i.e.,* the blank surface) and 1 represents the final point (*i.e.,* the saturated surface).

All sensorgrams obtained in the first three hours of PEG incubation are shown in **Fig. 7** for the three conditions. From kinetics data fitting adsorption rate constants (k_{ads}) and saturation time (*Time sat*) values were derived for all the tested species[44,46,47] (**Tab. 2**).

Biotin-PEG_{2kDa}-SH	**K_{ads} ($M^{-1}\times s^{-1}$)**	**Time sat. (h)**
w/o SAWs (@20.4°C)	(2.1±0.1) x 10^{-2}	22.51 ± 0.82
w/o SAWs (@32°C)	(7.5±0.1) x 10^{-2}	11.30 ± 0.28
w SAWs	(17.9±2.8) x 10^{-2}	4.07 ± 0.26
Avidin	**K_{ads} ($M^{-1}\times s^{-1}$)**	**Time sat. (min)**
w/o SAWs (@20.4°C)	5200 ± 1044	61.01 ± 0.64
w/o SAWs (@32°C)	6060 ± 1148	49.90 ± 0.44
w SAWs	6120 ± 858	46.32 ± 0.38

Tab. 2 Adsorption rate constants for bPEG2kDa-SH and avidin

View Article Online
DOI: 10.1039/C6LC00057F

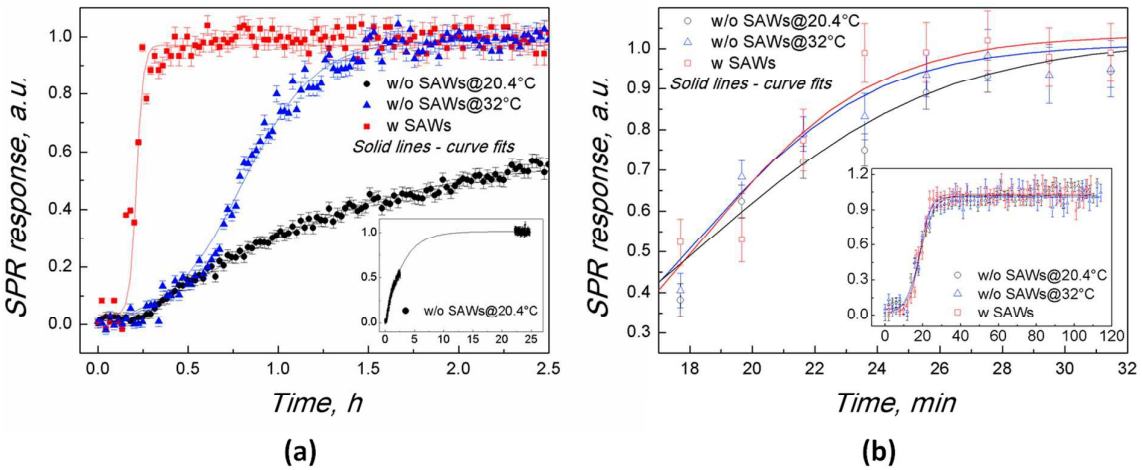

Fig. 7 SPR responses. **(a)** Comparison between biotin-PEG_{2kDa}-SH adsorption kinetics during 3 hours of PEG incubation obtained in the three experimental conditions: w/o SAWs@20.4°C (full black dots); w/o SAWs@32°C (full blue triangles); w SAWs (full red squares). In the inset PEG adsorption kinetics w/o SAWs@20.4°C is shown in a 24h-interval (measurements were acquired before and after night). Data were fitted using the thiol Langmuir adsorption kinetics tendency curve. **(b)** Comparison between avidin-biotin binding kinetics between 18 and 32 min of analyte incubation in the three experimental conditions: w/o SAWs@20.4°C (empty black dots); w/o SAWs@32°C (empty blue triangles); w SAWs (empty red squares). In the inset the complete avidin adsorption kinetics curves (110 min) are reported for all the experimental conditions tested. Data were fitted using a sigmoidal growth tendency curve.

k_{ads} of 2.1, 7.5 and 17.9 ($x\ 10^{-2}\ L\ x\ mol^{-1}\ x\ s^{-1}$) were calculated for biotin-PEG adsorption without SAWs, at 20.4 and 32°C, and with SAWs, respectively. In the presence of SAWs, the saturation time of PEG adsorption process is reduced from 22.49 to 4.07 h, and intermediate value of 11.26 h resulted from PEG adsorption at 32°C. In the case of avidin binding kinetics, k_{ads} of 5200, 6060 and 6120 ($L\ x\ mol^{-1}\ x\ s^{-1}$), corresponding to saturation times of 61, 50 and 46 min, without SAWs, at 20.4 and 32°C, and with SAWs, were obtained respectively.

The effective kinetics enhancement was quantitatively evaluated from K_{ads} and *Time sat* ratios, reported in **Fig. 8**. A ≈ 9-fold K_{ads} enhancement was obtained for the bPEG binding kinetics when passing from standard conditions to a SAW-driven reaction, while only a 3.6-fold enhancement was measured upon sensor heating at 32°C, leading to an 82% and 50% saturation time reduction, respectively. The experiment duration was decreased also for the avidin/biotin case: a $K_{ads} \approx 18\%$ enhancement when passing from standard conditions to SAWs-driven reactions, and $\approx 17\%$ enhancement when passing from standard to sensor heating conditions. In term of saturation times, 18% and 24% reductions were obtained upon sensor heating and SAW generation respectively. Clearly the results show that a strong acceleration of the kinetics in the case of slower reactions. Avidin-biotin extremely high affinity makes the kinetics reaction very quick and only a moderate relative increments of the absorption kinetics was achieved. On the contrary, in the case of the PEG the much slower reaction the acceleration is substantial.

View Article Online
DOI: 10.1039/C6LC00057F

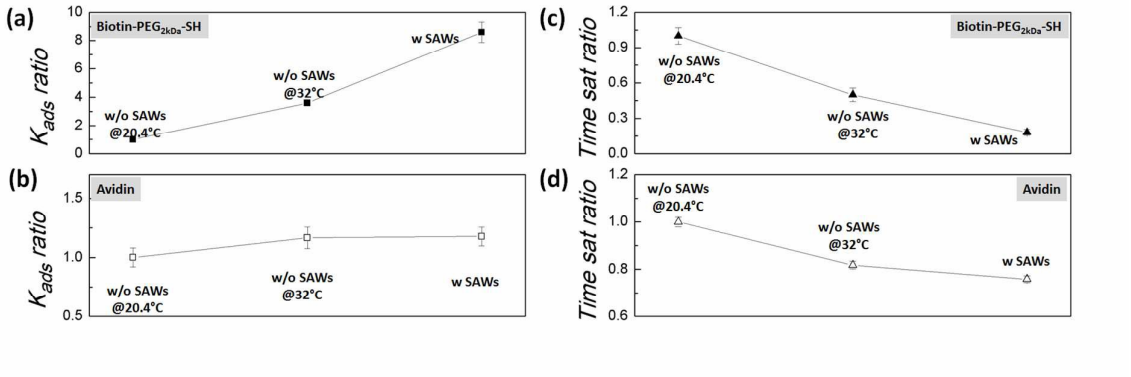

Fig. 8 Adsorption kinetics enhancements. K_{ads} trends by changing experimental conditions (w/o SAWs@20.4 and 32°C, and w SAWs) are shown for biotin-PEG2kDa-SH **(a)** and avidin **(b)** adsorption. Saturation time trends are reported in **(c)** and **(d)** for both PEG and avidin binding in all the experimental conditions tested.

4. Conclusions

Here, we developed a combined SPR-SAW microfluidic biosensor with enhanced binding kinetics driven by SAW-induced mixing. The device has been fully characterized in order to discern parasitic SAW heating effect with respect to the fluid stirring inside the microchamber that affects the molecules binding dynamics. This biochip works by exploiting Rayleigh SAWs generated on a LN substrate for the active mixing of biological solutions contained in a PDMS microfluidic chamber assembled onto nanostructured plasmonic sensing areas. The sensor response was detected using phase-interrogation SPR, here used for the first time in real-time by using a custom detection setup and dedicated software for data collection and processing. Avidin/biotin assay and thiol-polyethylene glycol (bPEG-SH) were exploited as model biological interaction and non-fouling layer respectively. SAW-induced biosensing kinetics enhancement in terms of time reduction resulted in a $\approx 82\%$ improvement for bPEG-SH adsorption onto gold and $\approx 24\%$ for avidin/biotin binding while heating alone only led to 50% and 18% improvement, respectively. These results demonstrated that, thanks to the SAW-induced mixing, our biochip can significantly reduce the experiment duration of bioreactions that usually require long times (*e.g.,* PEG-based sensing layer, low concentration analyte detection) that is a great impact on biological system and biosensing application as it significantly improve the experiment throughput. The sensing architecture here proposed represents a new promising SPR technology satisfying the major requirements of recent SPR technologies: scalability and high throughput. Indeed, the detection system size and biochip dimension can be further reduced and integrated into more complex chips; in addition, the possibility of reducing biological experiment duration via SAW-driven active mixing could be easily combined with the development of multiplexing platforms for parallel real-time sensing. In general, the technology reported in this study can be applied to a great variety of biological systems and sensing geometries basically formed by a thiol- or amino- probe anchored to the sensor surface (*e.g.,* nucleic acids, proteins, antibodies) and a specific analyte demonstrating the high versatility of the proposed approach.

Acknowledgements

View Article Online
DOI: 10.1039/C6LC00057F

This work has been supported by the "Nanotechnology-based therapy and diagnostics of brain diseases" project (NanoBrain - Progetto BANDIERA Nanomax) of Italian National Research Council. The authors also acknowledge Dr. Fabio Suran for the detection software development, Dr. Enrico Sovernigo for detection setup component fabrication support and Dr. Richie Shilton for the useful discussions and paper revision.

References

1. B. Liedberg, C. Nylander, and I. Lundström, *Biosens. Bioelectron.*, 1995, **10**, i–ix.

2. J. Homola, S. S. Yee, and G. Gauglitz, *Sensors Actuators B Chem.*, 1999, **54**, 3–15.

3. X. Wang, S. Zhan, Z. Huang, and X. Hong, *Instrum. Sci. Technol*., 2013, **41**, 574–607.

4. E. Ouellet, C. Lausted, T. Lin, C. W. T. Yang, L. Hood, and E. T. Lagally, *Lab Chip*, 2010, **10**, 581.

5. P. Chen, M. T. Chung, W. McHugh, R. Nidetz, Y. Li, J. Fu, T. T. Cornell, T. P. Shanley, and K. Kurabayashi, *ACS Nano*, 2015, 150323143413001.

6. J. Dostálek, H. Vaisocherová, and J. Homola, *Sensors Actuators B Chem.*, 2005, **108**, 758–764.

7. E. K. Sackmann, A. L. Fulton, and D. J. Beebe, *Nature*, 2014, **507**, 181–9.

8. P. Yager, T. Edwards, E. Fu, K. Helton, K. Nelson, M. R. Tam, and B. H. Weigl, *Nature*, 2006, **442**, 412–418.

9. G. M. Whitesides, *Nature*, 2006, **442**, 368–73.

10. C. Hansen and S. R. Quake, *Curr. Opin. Struct. Biol.*, 2003, **13**, 538–544.

11. T. M. Squires, R. J. Messinger, and S. R. Manalis, *Nat. Biotechnol.*, 2008, **26**, 417–426.

12. J. Friend and L. Y. Yeo, *Rev. Mod. Phys.*, 2011, **83**, 647–704.

13. G. De Simoni, G. Signore, M. Agostini, F. Beltram, and V. Piazza, *Biosens. Bioelectron.*, 2015, **68**, 570–576.

14. Y. Jiang, C. Y. Tan, S. Y. Tan, M. S. F. Wong, Y. F. Chen, L. Zhang, K. Yao, S. K. E. Gan, C. Verma, and Y.-J. Tan, *Sensors Actuators B Chem.*, 2015, **209**, 78–84.

15. J. Baca, V. Severns, D. Lovato, D. Branch, and R. Larson, *Sensors*, 2015, **15**, 8605–8614.

16. E. Gizeli, N. J. Goddard, C. R. Lowe, and A. C. Stevenson, *Sensors Actuators B Chem.*, 1992, **6**, 131–137.

17. J. Luo, P. Luo, M. Xie, K. Du, B. Zhao, F. Pan, P. Fan, F. Zeng, D. Zhang, Z. Zheng, and G. Liang, *Biosens. Bioelectron.*, 2013, **49**, 512–518.

18. T. Frommelt, M. Kostur, M. Wenzel-Schäfer, P. Talkner, P. Hänggi, and A. Wixforth, *Phys. Rev. Lett.*, 2008, **100**, 034502.

19. M. Travagliati, G. De Simoni, C. M. Lazzarini, V. Piazza, F. Beltram, and M. Cecchini, *Lab Chip*, 2012, **12**, 2621.

20. A. Wixforth, *Superlattices Microstruct.*, 2003, **33**, 389–396.

View Article Online
DOI: 10.1039/C6LC00057F

21. J. Kondoh, N. Shimizu, Y. Matsui, M. Sugimoto, and S. Shiokawa, *Sensors Actuators A Phys.*, 2009, **149**, 292–297.

22. R. J. Shilton, V. Mattoli, M. Travagliati, M. Agostini, A. Desii, F. Beltram, and M. Cecchini, *Adv. Funct. Mater.*, 2015, **25**, 5895–5901.

23. M. Cecchini, S. Girardo, D. Pisignano, R. Cingolani, and F. Beltram, *Appl. Phys. Lett.*, 2008, **92**.

24. M. Travagliati, R. J. Shilton, M. Pagliazzi, I. Tonazzini, F. Beltram, and M. Cecchini, *Anal. Chem.*, 2014, **86**, 10633–8.

25. J. Friend, L. Yeo, M. Tan, and R. Shilton, *Proc. - IEEE Ultrason. Symp.*, 2008, 014910, 930–933.

26. R. J. Shilton, M. Travagliati, F. Beltram, and M. Cecchini, *Adv. Mater.*, 2014, **26**, 4941–4946.

27. A. Renaudin, V. Chabot, E. Grondin, V. Aimez, and P. G. Charette, *Lab Chip*, 2010, **10**, 111–115.

28. B. H. Ha, K. S. Lee, G. Destgeer, J. Park, J. S. Choung, J. H. Jung, J. H. Shin and H. J. Sung, *Sci Rep.*, 2015, **5**, 11851.

29. F. Romanato, K. H. Lee, H. K. Kang, G. Ruffato and C. C. Wong, L., *Optics Express*, 2009, **17**, 12145

30. J. Homola, I. Koudela, and S. S. Yee, *Sensors Actuators B Chem.*, 1999, **54**, 16–24.

31. F. Romanato, K. H. Lee, G. Ruffato, and C. C. Wong, *Appl. Phys. Lett.*, 2010, **96**, 111103.

32. G. Ruffato, E. Pasqualotto, A. Sonato, G. Zacco, D. Silvestri, M. Morpurgo, A. De Toni, and F. Romanato, *Sensors Actuators B Chem.*, 2013, **185**, 179–187.

33. G. Ruffato and F. Romanato, *Opt. Lett.*, 2012, **37**, 2718–20.

34. A. Sonato, D. Silvestri, G. Ruffato, G. Zacco, F. Romanato, and M. Morpurgo, *Appl. Surf. Sci.*, 2013, **286**, 22–30.

35. H. Vaisocherová, E. Brynda, and J. Homola, *Anal. Bioanal. Chem.*, 2015, 3927–3953.

36. B. A. Auld, Acoustic Fields and Waves in Solids, John Wiley & Sons, New York, 1937.

38. M. G. Moharam, D. a. Pommet, E. B. Grann, and T. K. Gaylord, *J. Opt. Soc. Am. A*, 1995, **12**, 1077.

39. P. Lalanne and G. M. Morris, *J. Opt. Soc. Am. A*, 1996, **13**, 779–784.

40. P. T. T. Frommelt, D. Gogel, M. Kostur, *IEEE Trans.*, 2008, **55**, 2298 – 2305.

41. R. J. Shilton, L. Y. Yeo and J. R. Friend, *Sensors Actuators B. Chem.*, 2011, **160**, 1565–1572.

42. J. H. Grassi and R. M. Georgiadis, *Anal. Chem.*, 1999, **71**, 4392–6.

43. A. Meneghello, A. Antognoli, A. Sonato, G. Zacco, G. Ruffato, E. Cretaio and F. Romanato, *Anal. Chem.*, 2014, 86, 11773–11781.

44. D. Silvestri, A. Sonato, G. Ruffato, A. Meneghello, A. Antognoli, E. Cretaio, M. Dettin, A. Zamuner, E. Casarin, G. Zacco, F. Romanato, and M. Morpurgo, *Anal. Methods*, 2015, **7**, 4173-4180.

45. A. Sonato, G. Ruffato, G. Zacco, D. Silvestri, M. Natali, M. Carli, G. Giallongo, G. Granozzi, M. Morpurgo and F. Romanato, *Sensors Actuators B. Chem.*, 2011, 181, 559–566.

46. K. Hu and A. J. Bard, *Langmuir*, 1998, 7463, 4790–4794.

View Article Online
DOI: 10.1039/C6LC00057F

47. D. S. Karpovich and G. J. Blanchard, *Langmuir*, 1994, 3315–3322.